Ferroicity-Driven Nonlinear Photocurrent Switching in Time-Reversal Invariant Ferroic Materials

One Sentence Summary: First-principles study reveals that nonlinear photocurrent can be switched upon ferroic transition without breaking time-reversal symmetry.

Authors: Hua Wang[1], Xiaofeng Qian[1]*

Affiliations: [1]Department of Materials Science and Engineering, Texas A&M University, College Station, TX 77843, USA

*Corresponding author. Email: feng@tamu.edu (X.Q.)

Abstract:
Nonlinear optical responses to external electromagnetic field, characterized by second and higher order susceptibilities, play crucial roles in nonlinear optical devices and novel optoelectronics. Herein we demonstrate the possibility to achieve nonlinear photocurrent switching in time-reversal invariant multiferroics, namely ferroicity-driven nonlinear photocurrent switching. It is enabled by a Hall-like direct photocurrent originated from the second-order current response of time-reversal invariant systems to intense electromagnetic field whose direction can be controlled by both internal ferroic orders and external light polarization. Second-order direct photocurrent consists of two types of nonlinear responses – shift current and circular photocurrent under linearly and circularly polarized light irradiation dominated by topological shift vector and Berry curvature, respectively. We elucidate the microscopic mechanism of ferroicity-driven nonlinear photocurrent switching in a representative class of 2D multiferroic materials using group theoretical analyses and first-principles electronic structure theory. The complex interplay of crystalline, permutation, gauge, and time reversal symmetries as well as inherent causality governs the symmetry properties of shift current and circular photocurrent. Ferroicity-driven nonlinear photocurrent switching combined with rich ferroic degrees of freedom in multiferroic materials will open up a variety of new avenues for realizing tunable and configurable nonlinear optoelectronics, bulk photovoltaics, nonlinear multiferroics, etc. utilizing their ferroic orders and various nonlinear responses under external field.

MAIN TEXT:

INTRODUCTION

Nonlinear light-matter interaction plays a key role in the understanding, probing, and ultimate control of light and matter at the nanoscale. In particular, materials with strong nonlinear optical responses are highly desirable for many scientific disciplines and technological applications (*1-3*), e.g. ultrafast nonlinear optics (*4*) , nonlinear biosensing and imaging (*5*), efficient generation of entangled photon pairs for quantum computing and quantum sensing (*6, 7*), and all-optical transistor and computer (*8-10*). Due to the odd parity of the two polar vectors, electric dipole and electric field, even order nonlinear electrical susceptibility tensors vanish in centrosymmetric crystals (*11, 12*), while odd order responses are not limited by such constraint.

Among a plethora of optical responses, nonequilibrium direct current (DC) from periodically driven system under light field is of particular interest. One notable example is linear photovoltaic Hall effect which has been predicted in graphene (*13*). Additionally, there exist appealing second-order nonlinear DC responses to electromagnetic field in noncentrosymmetric solids, e.g. shift current (SC) and circular photocurrent (CC). Both were recently observed in Weyl semimetals (*14-18*). In parallel, recent experiments suggest two-dimensional van der Waals layered materials exhibit symmetry-dependent strong nonlinear optical responses, such as second/third harmonic generation. It makes nonlinear optical spectroscopy a perfect facile tool for characterizing and quantifying 2D materials, e.g. elastic strain, crystal orientation, phase transition, crystal thickness, even/odd layer oscillation, etc. Strong nonlinear responses in 2D materials also suggest their great advantage for phase-matching free nonlinear optics (*19-21*).

SC, known as bulk photovoltaic current (*22, 23*), refers to a photoexcitation of an electron from the valence to the conduction band with a simultaneous change in the phase of wave functions. Another type of nonlinear photocurrent, CC, also known as injection current, circular photogalvanic effect (CPGE) (*24, 25*) and quantum nonlinear optical Hall current (*26, 27*), arises from the interference of wavefunctions upon photoexcitation associated with a phase difference between two linearly polarized light, which allows for phase-modulated nonlinear photocurrent with tunable magnitude and direction. For example, left-circularly polarized and right-circularly polarized light can induce opposite currents. Using semiclassical Boltzmann framework, Moore et al. (*26*) and Sodemann et al. (*27*) revealed the fundamental roots of nonlinear SC and CC in Berry curvature induced anomalous velocity of metallic materials. This framework includes intraband process as the product of Berry phase and the gradient of Fermi-Dirac distribution function, equivalent to Berry curvature dipole (*27*). The nonlinear response in this case only considers the intraband process in metallic systems at the low frequency regime. In intrinsic semiconductors or insulators, the gradient of the Fermi-Dirac distribution and thus the Drude-like SC/CC response vanish. However, nonlinear photogalvanic current persists in non-centrosymmetric semiconductors due to nonlinear interband process which is absent in the above intraband model.

Herein we demonstrate the possibility to achieve nonlinear photocurrent switching in time-reversal invariant multiferroics, namely ferroicity-driven nonlinear photocurrent switching. More specifically, a Hall-like second-order direct photocurrent can be generated in time-reversal invariant systems upon electromagnetic field whose direction can be facilely controlled by both internal ferroic orders and external light polarization and chirality. We provide a microscopic picture based on first-principles theory and group theoretical analysis of crystalline symmetry, time reversal symmetry, permutation symmetry, gauge symmetry, and inherent causality. To illustrate the underlying mechanisms, we take monolayer group IV monochalcogenides (MX with M=Ge, Sn and X= S, Se, Te) as an example – a ferroelectric-ferroelastic multiferroics (*28, 29*). Experimentally, Chang et al. demonstrated that one of the MX compounds, atomic-thick SnTe, exhibits robust in-plane ferroelectricity at room temperature (*28*), and the application of

voltage pulse between the scanning tunneling microscope tip and monolayer SnTe can manipulate the ferroelectric polarization through domain wall motion. Our previous theoretical study also demonstrated a wide range of kinetic barriers for coherent ferroic transition and domain wall energies (*29*). These experimental and theoretical studies suggested that it is possible to realize ferroelectric/ferroelastic switching in MX monolayers. In this work, using first-principles calculations and group theoretical analyses we show that 2D MX monolayers exhibit large SC and CC responses that are dominated by topological quantities – shift vector and Berry curvature, respectively. More importantly, switching ferroelastic order flips the direction of nonlinear SC and CC photocurrent by ±90º, while switching ferroelectric orders flips both nonlinear photocurrents by 180º. In addition, changing left/right circular polarization of light will induce 180° flip in CC. The microscopic understanding of nonlinear photocurrent switching from first-principles theory, together with very recent discoveries of 2D ferroics/multiferroics as well as ferroelectric inorganic perovskites and hybrid organic-inorganic perovskites, will open a variety of new avenues for tunable and configurable nonlinear optoelectronics, bulk photovoltaics, and nonlinear multiferroics, etc.

RESULTS

Theory of SC and CC

Ferroicity-driven nonlinear photocurrent switching originates from the second-order photo-induced direct current density $\langle \boldsymbol{J}_{\mathrm{DC}} \rangle^{(2)}$. Unlike linear photocurrent, the direction of $\langle \boldsymbol{J}_{\mathrm{DC}} \rangle^{(2)}$ depends on intrinsic ferroic orders which is the key to ferroicity-driven nonlinear photocurrent switching. $\langle \boldsymbol{J}_{\mathrm{DC}} \rangle^{(2)}$ consists of two types of nonlinear photocurrents, SC and CC, which reflect the polarization change upon photoexcitation per unit volume,

$$\langle \boldsymbol{J}_{DC} \rangle^{(2)} = \langle \boldsymbol{J}_{SC} \rangle^{(2)} + \langle \boldsymbol{J}_{CC} \rangle^{(2)}, \tag{1}$$

where

$$\langle J^a_{SC} \rangle^{(2)} = 2\sigma_2^{abc}(0;\omega,-\omega)E^b(\omega)E^c(-\omega), \tag{2}$$

$$\frac{d\langle J^a_{\mathrm{CC}} \rangle^{(2)}}{dt} = -2\mathrm{Im}\,\eta_2^{abc}(0;\omega,-\omega)|E^b(\omega)||E^c(-\omega)|\sin(\varphi^b - \varphi^c). \tag{3}$$

Here a, b, c are Cartesian indices. The electric field can be described using phasors $\boldsymbol{E}(t) = \boldsymbol{E}(\omega)\exp(-i\omega t) + c.c.$ For linearly polarized light $\boldsymbol{E}(\omega)$ is real, while for left/right-circularly polarized light $\boldsymbol{E}(\omega)$ is complex, $E^b(\omega) = |E^b(\omega)|e^{i\varphi^b}$, with $\varphi^b - \varphi^c = \pm\frac{\pi}{2}$. We denote CC by $J^{a,\circlearrowleft}_{\mathrm{CC}}$ and $J^{a,\circlearrowright}_{\mathrm{CC}}$ for left and right-circularly polarized light, respectively, and denote SC by $J^{a,\leftrightarrow}_{\mathrm{SC}}$ and $J^{a,\updownarrow}_{\mathrm{SC}}$ for linearly x-/y-polarized light, respectively.

The SC susceptibility tensor σ_2^{abc} can be derived from perturbation theory (*25*) as

$$\sigma_2^{abc}(0;\omega,-\omega) = \frac{i\pi e^3}{2\hbar^2}\int[d\mathbf{k}]\sum_{nm\boldsymbol{\sigma}} f_{nm}\left(r^b_{mn}(r^c_{nm})_{;k^a} + r^c_{mn}(r^b_{nm})_{;k^a}\right)\delta(\omega_{mn}-\omega), \tag{4}$$

where $(r^b_{nm})_{;k^a} = \frac{\partial r^b_{nm}}{\partial k^a} - ir^b_{nm}(\mathcal{A}^a_n - \mathcal{A}^a_m)$ is the gauge covariant derivative. $\boldsymbol{r}_{nm} = i\langle n|\partial_{\boldsymbol{k}}|m\rangle$ and $\boldsymbol{\mathcal{A}}_n = i\langle n|\partial_{\boldsymbol{k}}|n\rangle$ are interband and intraband Berry connection, respectively. f is the Fermi-Dirac distribution with $f_{nm} \equiv f_n - f_m$, and $\hbar\Delta^a_{mn} \equiv v^a_{mm} - v^a_{nn}$ is the group velocity difference of band m and n. $[d\boldsymbol{k}] \equiv \frac{d\boldsymbol{k}}{(2\pi)^d}$ for d dimension. The SC susceptibility tensor under linearly polarized light can be rewritten in a more elegant expression,

$$\sigma_2^{abb}(0;\omega,-\omega) = -\frac{\pi e^3}{2\hbar^2}\int[d\mathbf{k}]\sum_{nm\boldsymbol{\sigma}} f_{nm}R^{a,b}_{nm}(\boldsymbol{k})r^b_{nm}r^b_{mn}\delta(\omega_{mn}-\omega), \tag{5}$$

where $R_{nm}^{a,b}(\boldsymbol{k}) = -\frac{\partial \phi_{nm}^{b}(\mathbf{k})}{\partial k^{a}} + \mathcal{A}_{n}^{a}(\boldsymbol{k}) - \mathcal{A}_{m}^{a}(\boldsymbol{k})$ is shift vector and $\phi_{nm}(\boldsymbol{k})$ is the phase factor of the Berry connection $r_{nm}^{b}(\boldsymbol{k}) = |r_{nm}^{b}(\boldsymbol{k})|e^{i\phi_{nm}^{b}(\boldsymbol{k})}$. $r_{nm}^{b}r_{mn}^{b}$ is the optical absorption strength. Hence, SC is determined by the product of linear photoabsorption and shift vector integrated over the Brillouin zone.

The CC susceptibility tensor η_2^{abc} (*25*) is given by

$$\eta_2^{abc}(0;\omega,-\omega) = -\frac{\pi e^3}{2\hbar^2}\int[d\boldsymbol{k}]\sum_{nm\boldsymbol{\sigma}}\Delta_{nm}^{a}f_{nm}[r_{mn}^{b},r_{nm}^{c}]\,\delta(\omega_{mn}-\omega), \tag{6}$$

where $[r_{mn}^{b},r_{nm}^{c}] \equiv r_{mn}^{b}r_{nm}^{c} - r_{mn}^{c}r_{nm}^{b}$, indicating CC vanishes under linearly polarized light. It can be rewritten in a general form assuming light propagates along z,

$$\eta_2^{a,z}(0;\omega,-\omega) = \frac{i\pi e^3}{2\hbar^2}\int[d\boldsymbol{k}]\sum_{nm\boldsymbol{\sigma}}f_{nm}\Delta_{nm}^{a}\Omega_{mn}^{z}(\boldsymbol{k})\delta(\omega_{mn}-\omega). \tag{7}$$

$\Omega_{mn}^{z}(\boldsymbol{k}) \equiv i\left[r_{mn}^{x},r_{nm}^{y}\right] = -i\left[r_{mn}^{y},r_{nm}^{x}\right]$ is local Berry curvature between band *m* and *n*. The global one reads $\Omega_{m}^{z} = \sum_{n\neq m}\Omega_{mn}^{z}$. It's clear to see $\eta_2^{abc} = -\eta_2^{acb}$. The original "*bc*" indices in the CC susceptibility tensor are now absorbed in the index "z".

SC and CC involve distinct physical processes. Figure 1 shows the corresponding microscopic picture using a two-band model. SC arises from the displacement of wave packet upon photoabsorption, while CC stems from the asymmetric transport of electrons and holes and the self-rotation of the wave packet. The latter induces orbital magnetic momentum coupled with the circularly polarized light. The intrinsic permutation symmetry of electric field leads to $\chi_2^{abc}(-\omega_m-\omega_n;\omega_m,\omega_n) = \chi_2^{acb}(-\omega_m-\omega_n;\omega_n,\omega_m)$, where χ_2^{abc} is a general second-order suseptibility. If time reversal symmetry is also present, $r_{nm}^{b}(-\boldsymbol{k}) = r_{mn}^{b}(\boldsymbol{k}), R_{nm}^{a,b}(-\boldsymbol{k}) = -R_{mn}^{a,b}(\boldsymbol{k}) = R_{nm}^{a,b}(\boldsymbol{k})$, $\boldsymbol{\Omega}_{mn}^{z}(\boldsymbol{k}) = -\boldsymbol{\Omega}_{mn}^{z}(-\boldsymbol{k})$. As a result of the causality and permutation symmetry, $\eta_2^{abc}(0;\omega,-\omega) = \eta_2^{acb}(0;-\omega,\omega) = -\eta_2^{abc}(0;-\omega,\omega) = [\eta_2^{abc}(0;-\omega,\omega)]^{*}$, ensuring η_2^{abc} is purely imaginary. In contrast, $\sigma_2^{abc}(0;\omega,-\omega) = \sigma_2^{acb}(0;-\omega,\omega) = \sigma_2^{abc}(0;-\omega,\omega) = [\sigma_2^{abc}(0;\omega,-\omega)]^{*}$, suggesting σ_2^{abc} is purely real.

Relation between SC and CC

Although SC and CC have different physical meaning, they are closely related. The derivative of CC susceptibility tensor $\eta_2^{a,z}$ in Eq. 7 can be written as the following

$$\partial_{\omega}\eta_2^{a,z}(0;\omega,-\omega) = \frac{i\pi e^3}{2\hbar^2}\int[d\boldsymbol{k}]\sum_{nm\boldsymbol{\sigma}}f_{nm}(\partial_{k^{a}}\Omega_{mn}^{z})\,\delta(\omega_{mn}-\omega), \tag{8}$$

where the integration by parts is applied. Here $\partial_{k^{a}}\Omega_{mn}^{z}$ is the Berry curvature dipole. Furthermore,

$$\nabla_{\boldsymbol{k}}\times\boldsymbol{R}_{mn}\cdot\hat{\boldsymbol{z}} = \frac{\partial R_{mn}^{y,a}(\boldsymbol{k})}{\partial k^{x}} - \frac{\partial R_{mn}^{x,a}(\boldsymbol{k})}{\partial k^{y}} = \Omega_{m}^{z} - \Omega_{n}^{z}. \tag{9}$$

It shows that the two topological quantities, shift vector and Berry curvature, are closely connected. For a two-band model, $\Omega_{m}^{z} - \Omega_{n}^{z} = 2\Omega_{mn}^{z}$, thus

$$\partial_{\omega}\eta_2^{a,z}(0;\omega,-\omega) = \frac{-i\pi e^3}{4\hbar^2}\int[d\boldsymbol{k}]\sum_{\boldsymbol{\sigma}}\nabla_{k^{a}}(\nabla_{\boldsymbol{k}}\times\boldsymbol{R}_{vc}\cdot\hat{\boldsymbol{z}})\,\delta(\omega_{cv}-\omega). \tag{10}$$

Therefore, both SC and the derivative of CC with respect to frequency are related to the shift vector, hence the Berry curvature. The derivative of susceptibility $\partial_{\omega}\eta_2^{a,z}$ will contribute to the temporal response of rectification current rate when a short laser pulse is applied (*30*).

First-principles calculation and group theoretical analysis of SC in 2D multiferroic MX

The symmetry property of linear susceptibility and nonlinear SC and CC susceptibility are governed by point group and permutation symmetry, which correspond to direct product $\Gamma_{\boldsymbol{P}}\otimes\Gamma_{\boldsymbol{E}}$, $\Gamma_{\boldsymbol{J_{SC}}}\otimes\Gamma_{\boldsymbol{EE}}$, $\Gamma_{\boldsymbol{J_{CC}}}\otimes\Gamma_{\boldsymbol{E\times E^{*}}}$, respectively. Here we take monolayer group IV monochalcogenides (MX with M=Ge, Sn and X=Se, S) as an example which is a ferroelectric-ferroelastic multiferroics (*29*). In 2D MX with C_{2v} point group (see

Figs. 2A and 2B for crystal and electronic structure, respectively) and its character table (Table S1), we have $\Gamma_{\boldsymbol{P}}\otimes\Gamma_{\boldsymbol{E}} = 3A_1 + 2A_2 + 2B_1 + 2B_2$. Hence there are three independent nonzero components in linear susceptibilities. The permutation symmetry further separates them into symmetric and asymmetric representations (*31*), $\Gamma_{\boldsymbol{P}}\otimes\Gamma_{\boldsymbol{E}} = \Gamma^s + \Gamma^a$, where $\Gamma^s = 3A_1 + A_2 + B_1 + B_2$ and $\Gamma^a = A_2 + B_1 + B_2$. Moreover, since polarization $\boldsymbol{P}$, current $\boldsymbol{J}$, and electric field $\boldsymbol{E}$ are all polar vectors, they share the same representation, thus $\Gamma_{\mathbf{Jsc}}\otimes\Gamma_{\boldsymbol{EE}} = 7A_1 + 6A_2 + 7B_1 + 7B_2$, and $\Gamma_{\mathbf{Jsc}}\otimes\Gamma^s_{\boldsymbol{EE}} = 5A_1 + 3A_2 + 5B_1 + 5B_2$. As a result, there are five independent nonzero components in the SC susceptibility tensor. Figures 2C and 2D show two of the five nontrivial frequency dependent SC susceptibilities $\sigma_2^{yxx}(0;\omega,-\omega)$ and $\sigma_2^{yyy}(0;\omega,-\omega)$ in 2D MX where linearly x- and y-polarized light are considered. The corresponding SC along y direction reads $J_{\mathrm{SC}}^{y,\leftrightarrow} = 2\,\sigma_2^{yxx}E^xE^x$ and $J_{\mathrm{SC}}^{y,\updownarrow} = 2\,\sigma_2^{yyy}E^yE^y$, respectively. The SC for monolayer GeS agrees well with the results in Refs. (*21, 32*). Furthermore, as shown in Fig. 2C and 2D, spin-orbit coupling (SOC) only slightly affects the SC in the case of GeS because of weak spin-orbit interaction strength of Ge and S atoms. σ_2^{yyy} has two peaks below frequency of 3 eV. The first peak at 2 eV (denoted by red circle in Fig. 2C) is contributed from the k-points around the Brillouin zone center (Γ point). The second peak at 2.8 eV denoted by green circle is apparently very strong. It comes from the transition at the k-points around the Brillouin zone boundary (X point) in a butterfly shape as shown in Fig. 2C. However, SOC can have significant impact in other cases such as well-known 1H-$MoSe_2$ and WSe_2, and the results for all MX and MX_2 without and with SOC are shown in Figs. S1 and S2 in the Supplementary Materials, respectively.

The reciprocal vector dependent contributions to SC are shown in Figs. 2E and 2F for photon energy of 2.0 and 2.8 eV, respectively. They are determined by the product of SC susceptibility density, $\mathrm{Im}\left[r^b_{vc}r^b_{cv;k^a}\right]$ (Figs. 2G and 2J for 2.0 and 2.8 eV, respectively), and the energy conservation law is carried by $\delta(\omega_{cv}-\omega)$. The distribution of shift current susceptibility density can be further understood by focusing on the frequency independent terms determined by the product of dipole transition strength, $r^b_{vc}r^b_{cv}$ (*i.e.* optical absorption), and shift vector $R^{a,b}_{nm}(\boldsymbol{k})$, as shown in Figs. 2H-2I and 2K-2L, for 2.0 and 2.8 eV, respectively. Im $r^x_{vc}r^x_{cv}$ vanishes at the k points around the band gap, while Im $r^y_{vc}r^y_{cv}$ remains finite due to the optical selection rule. $R^{a,b}_{nm}(\boldsymbol{k})$ is a gauge invariant topological quantity which is well defined away from optical zero points, *i.e.* $r^b_{nm}(\boldsymbol{k}) \neq 0$. Since the optical zero points have no contribution to SC, we compute the shift vector by

$$R^{a,b}_{nm}(\boldsymbol{k}) = \frac{1}{|r^b_{nm}|^2}\mathrm{Im}\left[r^b_{mn}r^b_{nm;k^a}\right]. \tag{11}$$

The quantitative relationship between shift vector and polarization difference was recently reported (*33*). In the presence of time reversal symmetry, $r^b_{nm}(-\boldsymbol{k}) = r^b_{mn}(\boldsymbol{k}), \left(r^b_{nm}(-\boldsymbol{k})\right)_{;k^a} = -\left(r^b_{mn}(\boldsymbol{k})\right)_{;k^a}$, which leads to $R^{a,b}_{nm}(-\boldsymbol{k}) = -R^{a,b}_{mn}(\boldsymbol{k}) = R^{a,b}_{nm}(\boldsymbol{k})$. This is clearly confirmed in Figs. 2I and 2L. The shift vector can reach as high as ~15 Å, much larger than its lattice constant. This is very different from electric polarization vector which is smaller than the lattice vector. Figures S3 and S4 show the distribution of the SC susceptibility tensor elements for monolayer $MoSe_2$ in the first Brillouin zone, demonstrating that its shift vector defined in Eq. 11 can go beyond its lattice parameter.

First-principles calculation and group theoretical analysis of CC in 2D multiferroic MX

For circularly polarized light along z, $(\boldsymbol{E}\times\boldsymbol{E}^*)_z$ and axial axis R_z share the B_2 representation. Therefore, $\Gamma_{j^x}\otimes\Gamma_{R_z} = B_2\otimes B_2 = A_1$, indicating there is a nonzero CC response along x direction $\eta_2^{x,z}(0;\omega,-\omega)$ when the applied circularly polarized light is along z direction, *i.e.* perpendicular to 2D plane. Figures 3A and 3B show two antisymmetric CC susceptibility tensor elements, Im η_2^{xxy} and Im η_2^{xyx}, respectively. Unlike SC, the main response of CC spread in two peaks from 2 to 6 eV. The peak values of Im η_2^{abc} in

the four MX materials are about $100 \sim 300 \times 10^8$ nm $AV^{-2}s^{-1}$, which allows us to estimate the generated nonlinear circular current under continuous wave limit as follows. At room temperature, a typical relaxation time of the electrons in MX materials is around $\tau = \mu_e/(\frac{e}{m^*}) \sim 10^{-14}s$ (*34*). μ_e is the mobility and m^* is the effective mass of electrons. Considering a regular laser pointer with an intensity of 1mW/cm^2 and 2D MX with an effective thickness of 1nm, the induced circular photocurrent J_{CC} can reach $10 \sim 30\mu A/cm^2$, indicating the current can even be observed using low power continuous wave source (sheet photocurrent of $10 \sim 30$ nm$\frac{\mu A}{cm^2}$, that is, $100 \sim 300 pA/m$) (*35*). SC and CC are generated simultaneously under circularly polarized light. It is possible to compare their peak amplitudes if we assume the same incident light intensity and a relaxation time of $10^{-14}s$ for GeS. CC is larger than SC, J_{CC}/J_{SC} =~5. The second-order nonlinear photocurrent response for different incident polarized light is summarized in Table S2. It should be noted that there is another nonzero element $\eta_2^{z,x}(0;\omega,-\omega)$ in the CC susceptibility tensor since $\Gamma_{j^z} \otimes \Gamma_{R_x} = B_1 \otimes B_1 = A_1$, suggesting there exists a CC response along z direction when the incoming circularly polarized light is along x direction.

Figures 3C and 3D show the $\boldsymbol{k}$ resolved CC susceptibility in monolayer GeS under circularly polarized light at two different frequencies (2.3 and 2.8 eV), demonstrating that the main response of the CC is localized around Y point. It should be noted that, for the same frequency of 2.8 eV, the SC (Fig. 2F) and CC (Fig. 3D) are very different from each other, as the SC is localized around Y point. The CC susceptibility is determined by the product of group velocity difference and Berry curvature $\boldsymbol{\Omega}_{cv}^z(\boldsymbol{k})$. The susceptibility tensor relates the component of the polar vector $\boldsymbol{J}$ and the axial vector $\mathbf{e}\times\mathbf{e}^*$. Hence, it is nonzero for the point groups that allow optical activity or gyrotropy. Here $\mathbf{e}$ is the unit vector of light polarization. Figure 3E shows the group velocity difference between the highest valence band and the lowest conduction band, which confirms the time reversal symmetry $\boldsymbol{\Delta}(\boldsymbol{k}) = -\boldsymbol{\Delta}(-\boldsymbol{k})$ (see Figs. S5 and S6 for the energy-dependent group velocity distribution). The Berry curvature $\boldsymbol{\Omega}_{cv}^z(\boldsymbol{k})$ of GeS is shown in Fig. 3F, which confirms $\boldsymbol{\Omega}_{cv}^z(\boldsymbol{k}) = -\boldsymbol{\Omega}_{cv}^z(-\boldsymbol{k})$ under time reversal symmetry and the mirror plane (yz-plane) leads to opposite Berry curvature at $(\pm k^x, k^y)$. The product of these two odd functions, $\boldsymbol{\Delta}(\boldsymbol{k})$ and $\boldsymbol{\Omega}_{cv}^z(\boldsymbol{k})$, results in nonvanishing CC in 2D MX with C_{2v} point group. This is in direct constrast to 1H-$MoSe_2$ whose CC response vanishes due to its D_{3h} point group (see character table in Table S1) as evident in its Berry curvature shown in Fig. S7.

Ferroicity-driven nonlinear photocurrent switching

The above group theoretical analyses and first-principles calculations illustrate the underlying selection rule and microscopic mechanism governing nonlinear SC and CC photocurrents. Since they are intimately related to the symmetry and topology, nonlinear SC and CC photocurrents are inherently coupled with the intrinsic ferroic orders in 2D multiferroics MX, giving rise to ferroicity-driven nonlinear photocurrent switching which we will discuss below. Let's first inspect the coupling between ferroelectric order (P_y) and nonlinear SC and CC responses. Since both CC and SC are polar vector, the sign of SC will flip upon ferroelectric polarization switch ($P_y \rightarrow -P_y$). Consequently, the sign of SC susceptibility tensor $\sigma_2^{ybb}(0;\omega,-\omega)$ and CC susceptibility tensor $\eta_2^{x,z}(0;\omega,-\omega)$ will also flip. Thus, under the same linearly/circularly polarized light, SC and CC will change the direction by 180° upon ferroelectric polarization switch, that is, $J_{SC}^{y,\leftrightarrow}(P_y) = -J_{SC}^{y,\leftrightarrow}(-P_y)$, $J_{SC}^{y,\updownarrow}(P_y) = -J_{SC}^{y,\updownarrow}(-P_y)$, $J_{CC}^{x,\circlearrowleft}(P_y) = -J_{CC}^{x,\circlearrowleft}(-P_y)$, and $J_{CC}^{x,\circlearrowright}(P_y) = -J_{CC}^{x,\circlearrowright}(-P_y)$. Such property can be obtained from microscopic theory by considering the transformation rules of different matrix elements under space inversion and time reversal operation, including inter-band Berry connections $\boldsymbol{r}_{mn}(\boldsymbol{k})$, shift vector $\boldsymbol{R}_{mn}(\boldsymbol{k})$, group velocity difference $\boldsymbol{\Delta}_{mn}(\boldsymbol{k})$, and Berry curvature $\boldsymbol{\Omega}_{mn}(\boldsymbol{k})$ as listed in Table 1.

Next we examine the coupling between ferroelastic order (e.g. spontaneous strain $\epsilon_{yy} > 0$ and $\epsilon_{xx} < 0$) and nonlinear photocurrent responses. Upon ferroelastic transition ($\epsilon_{yy} \rightarrow \epsilon_{xx}$ and $\epsilon_{xx} \rightarrow \epsilon_{yy}$), shift vector $R^{y,b}_{nm}(\boldsymbol{k})$, Berry curvature $\Omega^{z}_{mn}(\boldsymbol{k})$, $r^{b}_{nm}r^{b}_{mn}$ and Δ^{a}_{nm} will all rotate by 90°, which effectively switches the xy index. As a result, under the same linearly/circularly polarized light, nonlinear SC and CC photocurrent will change their direction by 90° upon ferroelastic transition, that is, $J^{y,\leftrightarrow}_{\mathrm{SC}}(\epsilon_{yy}) = J^{x,\updownarrow}_{\mathrm{SC}}(\epsilon_{xx})$, $J^{y,\updownarrow}_{\mathrm{SC}}(\epsilon_{yy}) = J^{x,\leftrightarrow}_{\mathrm{SC}}(\epsilon_{xx})$, $J^{y,\circlearrowleft}_{\mathrm{CC}}(\epsilon_{yy}) = J^{x,\circlearrowleft}_{\mathrm{CC}}(\epsilon_{xx})$, and $J^{x,\circlearrowright}_{\mathrm{CC}}(\epsilon_{yy}) = J^{x,\circlearrowright}_{\mathrm{CC}}(\epsilon_{xx})$. Note that in general $J^{\circlearrowleft}_{\mathrm{CC}} = -J^{\circlearrowright}_{\mathrm{CC}}$, $J^{y,\leftrightarrow}_{\mathrm{SC}}$, and $J^{y,\updownarrow}_{\mathrm{SC}}$ are independent. However, $J^{y,\leftrightarrow}_{\mathrm{SC}} = -J^{y,\updownarrow}_{\mathrm{SC}}$ holds in group D_{3h} with a mirror plane perpendicular to *x* axis, e.g. 1H-$MoSe_2$.

Since 2D MX possess both ferroelectric and ferroelastic orders, it has four multiferroic $(\pm P, \pm\epsilon)$ states whose nonlinear photocurrent SC and CC are directly correlated as listed in Table 2. Here we define ferroelastic strain $+\epsilon$ for $\epsilon_{xx} < 0$ and $\epsilon_{yy} > 0$, and $-\epsilon$ for $\epsilon_{xx} > 0$ and $\epsilon_{yy} < 0$. Ferroelectric polarization *P* could be $\pm P_x$ if $\epsilon_{xx} > 0$, or $\pm P_y$ if $\epsilon_{yy} > 0$. In contrast, linear optical susceptibility will not change with ferroelectric polarization switching because its matrix element $r^{b}_{nm}r^{b}_{mn}$ is always positive. Moreover, for a given multiferroic state (P, ϵ), nonlinear SC and CC current responses in 2D MX are bulk photocurrent response along different directions, thus SC and CC can serve as a fundamental principle for real-space mapping of ferroelectric and ferroelastic orders.

DISCUSSION

The above group theoretical analysis and first-principles calculations can be generally applied to other ferroic materials that can host ferroicity-driven nonlinear photocurrent switching. We can extend the above analysis to all 32 crystallographic point groups. 21 are noncentrosymmetric point groups, 10 of which $(\mathrm{C}_1, \mathrm{C}_s, \mathrm{C}_n, \mathrm{C}_{nv}, n = 2,3,4,6)$ possess polar axis – a necessary but insufficient condition for ferroelectric materials. Assuming z to be the polar axis, z will transform as the total symmetric representation, therefore $\Gamma_{j^z} \otimes \Gamma_{E^x} \otimes \Gamma_{E^x}$ and $\Gamma_{j^z} \otimes \Gamma_{E^y} \otimes \Gamma_{E^y}$ always contain the total symmetric representation, indicating that nonvanishing SC is perpendicular to electric field and thus leads to a nonlinear transverse photocurrent. Such transverse current cannot be observed from conventional linear Hall effect in time-reversal invariant materials. Furthermore, 18 of 21 noncentrosymmetric point groups including all the 10 polar classes are gyrotropic, hence they all possess nonvanishing CC.

Although our focus here is on the ferroicity-driven nonlinear photocurrent switching based on interband-process induced second-order photocurrent, the similar effect can be also found in ferroelectric semimetals where static/low-frequency electric field induced nonlinear Hall current can be switched upon ferroelectric switching. However, it should be emphasized that not all ferroic materials exhibit nonlinear photocurrent switching upon ferroic transition. Similar to the present case, it depends on the underlying symmetry transformation of ferroelectric transition. More excitingly, it can be readily extended to higher-order or other types of nonlinear effects, for examples, optically induced nonlinear magnetization switching and ferroicity-driven third-order nonlinear photocurrent switching. It will offer unprecedented opportunities for nonlinear optoelectronics, nonlinear optomagnetics, and nonlinear optoelectromagnetics, namely nonlinear multiferroics, as potential routes to control polarization, charge current, magnetization, and spin current in an ultrafast, noninvasive manner without the stringent requirement of strongly-coupled lattice, polarization, and magnetization in conventional multiferroics.

In summary, using group theoretical analyses and first-principles calculations we have studied the microscopic mechanism of nonlinear photocurrent switching in time-reversal invariant multiferroics. Our results show that nonlinear photocurrent is highly senstive to the symmetry of materials, including point

group symmetry, permutation symmetry, and time reversal symmetry. This leads to ferroicity-driven nonlinear photocurrent switching – unique to multiferroics where the direction of second-order photocurrent is strongly correlated with intrinsic ferroic orders and external light polarization. The concept of ferroicity-driven nonlinear photocurrent switching illustrated here is not limited to 2D multiferroics, rather it can be generally applicable to many ferroics (e.g. ferroelectric inorganic perovskites and hybrid organic-inorganic perovskites) and even ferroelectric metals. One can envisage to directly control nonlinear photocurrent by switching ferroelastic strain and/or ferroelectric polarization accompanied by instantaneous direction and/or sign switching of the photocurrent. Furthermore, one may conduct high-resolution characterization of ferroelastic and ferroelectric orders as well as domain evolution using ultrafast optical techniques based on ferroicity-dependent nonlinear photocurrent. The present findings thus will open up avenues for realizing configurable nonlinear optoelectronics, bulk photovoltaics, nonlinear multiferroics, etc. utilizing their ferroic orders and various nonlinear responses under external field.

MATERIALS AND METHODS

First-principles atomistic and electronic structure calculations

Ground-state crystal structures of MX were calculated by first-principles density-functional theory (*36, 37*) implemented in the Vienna Ab initio Simulation Package (VASP) (*38, 39*) with the projector-augmented wave method (*40*) and a plane-wave basis with an energy cutoff of 400 eV. We employed the generalized-gradient approximation of exchange-correlation functional in the Perdew-Burke-Ernzerhof (*41*) form and a Monkhorst-Pack k-point sampling of 12×12×1 for the Brillouin zone integration.

First-principles nonlinear shift current and circular photocurrent

To evaluate the nonlinear photocurrent responses, we developed a nonlinear optical code interfaced with first-principles density functional theory packages (e.g. VASP and Quantum-ESPRESSO). Second-order nonlinear photocurrent responses such as SC and CC are different from linear optical absorption, as the numerical integration of generalized Berry connection has to be performed over the whole Brillouin zone and multiple band indices for 27 third-rank tensor elements at each frequency. We therefore parallelized and benchmarked the code with tensor symmetrization and SOC taken into account. For the present calculations, we found that a dense 72x72x1 k-point sampling, 40 electronic bands without SOC (80 bands with SOC), and total 1000 frequency grids in an energy range of [-6 eV, 6 eV] are enough to achieve converged nonlinear photocurrent susceptibility tensors. The fundamental frequency ω in the denominator of susceptibility tensor carries a small imaginary smearing factor τ of 0.05 eV: $\omega \to \omega + i\tau$. We used the Sokhotski-Plemelj theorem to perform the integrals of Dirac delta function, which reads $\lim_{\tau\to 0} \frac{1}{\omega_{mn} \pm (\omega + i\tau)} = \mathcal{P}\frac{1}{\omega_{mn} \pm \omega} \mp i\pi\delta(\omega_{mn} \pm \omega)$. $\mathcal{P}$ is the Cauchy principal value. It should be emphasized that this formula is only meaningful when it is multiplied by a function and integrated over the first Brillouin zone and the real line that includes the point $\omega = \omega_{mn}$. This always holds true in our case. Finally, the single-particle approximation often underestimates the bandgap, and two-body and higher-order interactions may also affect the results. To check the effect of the single-particle approximation, we applied a scissor operator to correct both bandgap and matrix elements by using the optical bandgap obtained from quasiparticle GW and Bethe-Salpeter equation calculations. This approach is a reasonable remedy as the GW and DFT band structures are similar for the MX materials. Figure S8 shows the nonlinear photocurrent calculated with and without the scissor operator, and the main effect is the relative shift of the peak positions with slightly reduced peak intensity. This is expected as it mostly affects the denominator and delta function in the equations for SC and CC. Two-body and higher-order excitations in principle can be taken into account by incorporating many-body wavefunctions (e.g. exciton wavefunctions as a linear combination of

electron-hole pair excitations) into the SC and CC tensor, which may change the SC and CC peak position and amplitude. Nonetheless, the main conclusions on the ferroicity-driven nonlinear photocurrent switching behavior from the symmetry analysis and first-principles calculations shall still hold, and future efforts shall be made to include the exciton and other high-order excitation effect.

REFERENCES AND NOTES

1. J. Weiner, F. Nunes, *Light-Matter Interaction: Physics and Engineering at the Nanoscale*. (OUP Oxford, 2012).
2. C. Lienau, M. A. Noginov, M. Lončar, Light–matter interactions at the nanoscale. *Journal of Optics* **16**, 110201 (2014).
3. J. Weiner, P.-T. Ho, *Light-matter Interaction, Fundamentals and Applications*. (John Wiley & Sons, 2008), vol. 1.
4. R. Thomson, C. Leburn, D. Reid, *Ultrafast Nonlinear Optics*. (Springer, 2013).
5. C. L. Evans, X. S. Xie, Coherent anti-Stokes Raman scattering microscopy: chemical imaging for biology and medicine. *Annu. Rev. Anal. Chem.* **1**, 883-909 (2008).
6. P. G. Kwiat, E. Waks, A. G. White, I. Appelbaum, P. H. Eberhard, Ultrabright source of polarization-entangled photons. *Phys. Rev. A* **60**, R773-R776 (1999).
7. N. Gisin, G. Ribordy, W. Tittel, H. Zbinden, Quantum cryptography. *Rev. Mod. Phys.* **74**, 145-195 (2002).
8. M. F. Yanik, S. Fan, M. Soljačić, J. D. Joannopoulos, All-optical transistor action with bistable switching in a photonic crystal cross-waveguide geometry. *Opt. Lett.* **28**, 2506-2508 (2003).
9. V. R. Almeida, C. A. Barrios, R. R. Panepucci, M. Lipson, All-optical control of light on a silicon chip. *Nature* **431**, 1081-1084 (2004).
10. C. Ríos, M. Stegmaier, P. Hosseini, D. Wang, T. Scherer, C. D. Wright, H. Bhaskaran, W. H. P. Pernice, Integrated all-photonic non-volatile multi-level memory. *Nat. Photon.* **9**, 725-732 (2015).
11. Y.-R. Shen, *The Principles of Nonlinear Optics*. New York, Wiley-Interscience (1984).
12. R. W. Boyd, *Nonlinear Optics*. (Elsevier Inc., ed. 3rd, 2008).
13. T. Oka, H. Aoki, Photovoltaic Hall effect in graphene. *Phys. Rev. B* **79**, 081406 (2009).
14. L. Wu, S. Patankar, T. Morimoto, N. L. Nair, E. Thewalt, A. Little, J. G. Analytis, J. E. Moore, J. Orenstein, Giant anisotropic nonlinear optical response in transition metal monopnictide Weyl semimetals. *Nat. Phys.* **13**, 350-355 (2017).
15. T. Morimoto, N. Nagaosa, Topological nature of nonlinear optical effects in solids. *Science Advances* **2**, e1501524 (2016).
16. G. B. Osterhoudt, L. K. Diebel, M. J. Gray, X. Yang, J. Stanco, X. Huang, B. Shen, N. Ni, P. J. W. Moll, Y. Ran, K. S. Burch, Colossal mid-infrared bulk photovoltaic effect in a type-I Weyl semimetal. *Nat. Mater.*, (2019).
17. F. de Juan, A. G. Grushin, T. Morimoto, J. E. Moore, Quantized circular photogalvanic effect in Weyl semimetals. *Nat. Commun.* **8**, 15995 (2017).
18. Q. Ma, S.-Y. Xu, C.-K. Chan, C.-L. Zhang, G. Chang, Y. Lin, W. Xie, T. Palacios, H. Lin, S. Jia, Direct optical detection of Weyl fermion chirality in a topological semimetal. *Nat. Phys.* **13**, 842 (2017).
19. M. Zhao, Z. Ye, R. Suzuki, Y. Ye, H. Zhu, J. Xiao, Y. Wang, Y. Iwasa, X. Zhang, Atomically phase-matched second-harmonic generation in a 2D crystal. *Light: Science and Applications* **5**, e16131 (2016).
20. H. Wang, X. Qian, Giant Optical Second Harmonic Generation in Two-Dimensional Multiferroics. *Nano Lett.* **17**, 5027-5034 (2017).
21. T. Rangel, B. M. Fregoso, B. S. Mendoza, T. Morimoto, J. E. Moore, J. B. Neaton, Large Bulk Photovoltaic Effect and Spontaneous Polarization of Single-Layer Monochalcogenides. *Phys. Rev.*

Lett. **119**, 067402 (2017).
22. R. von Baltz, W. Kraut, Theory of the bulk photovoltaic effect in pure crystals. *Phys. Rev. B* **23**, 5590-5596 (1981).
23. S. M. Young, A. M. Rappe, First Principles Calculation of the Shift Current Photovoltaic Effect in Ferroelectrics. *Phys. Rev. Lett.* **109**, 116601 (2012).
24. P. J. Sturman, V. M. Fridkin, *Photovoltaic and Photo-refractive Effects in Noncentrosymmetric Materials*. (CRC Press, 1992), vol. 8.
25. J. E. Sipe, A. I. Shkrebtii, Second-order optical response in semiconductors. *Phys. Rev. B* **61**, 5337-5352 (2000).
26. J. E. Moore, J. Orenstein, Confinement-Induced Berry Phase and Helicity-Dependent Photocurrents. *Phys. Rev. Lett.* **105**, 026805 (2010).
27. I. Sodemann, L. Fu, Quantum Nonlinear Hall Effect Induced by Berry Curvature Dipole in Time-Reversal Invariant Materials. *Phys. Rev. Lett.* **115**, 216806 (2015).
28. K. Chang, J. Liu, H. Lin, N. Wang, K. Zhao, A. Zhang, F. Jin, Y. Zhong, X. Hu, W. Duan, Q. Zhang, L. Fu, Q.-K. Xue, X. Chen, S.-H. Ji, Discovery of robust in-plane ferroelectricity in atomic-thick SnTe. *Science* **353**, 274-278 (2016).
29. H. Wang, X. Qian, Two-dimensional multiferroics in monolayer group IV monochalcogenides. *2D Mater.* **4**, 015042 (2017).
30. F. Nastos, J. Sipe, Optical rectification and shift currents in GaAs and GaP response: Below and above the band gap. *Physical Review B* **74**, 035201 (2006).
31. M. S. Dresselhaus, G. Dresselhaus, A. Jorio, *Group theory: application to the physics of condensed matter*. (Springer Science & Business Media, 2007).
32. C. Wang, X. Liu, L. Kang, B.-L. Gu, Y. Xu, W. Duan, First-principles calculation of nonlinear optical responses by Wannier interpolation. *Physical Review B* **96**, 115147 (2017).
33. B. M. Fregoso, T. Morimoto, J. E. Moore, Quantitative relationship between polarization differences and the zone-averaged shift photocurrent. *Physical Review B* **96**, 075421 (2017).
34. O. Madelung, *Semiconductors—basic data*. (Springer Science & Business Media, 2012).
35. N. Laman, A. Shkrebtii, J. Sipe, H. Van Driel, Quantum interference control of currents in CdSe with a single optical beam. *Appl. Phys. Lett.* **75**, 2581-2583 (1999).
36. P. Hohenberg, W. Kohn, Inhomogeneous electron gas. *Phys. Rev. B* **136**, B864-B871 (1964).
37. W. Kohn, L. J. Sham, Self-consistent equations including exchange and correlation effects. *Phys. Rev.* **140**, A1133-A1138 (1965).
38. G. Kresse, J. Furthmüller, Efficient iterative schemes for *ab initio* total-energy calculations using a plane-wave basis set. *Phys. Rev. B* **54**, 11169-11186 (1996).
39. G. Kresse, J. Furthmüller, Efficiency of ab-initio total energy calculations for metals and semiconductors using a plane-wave basis set. *Comput. Mater. Sci.* **6**, 15-50 (1996).
40. P. E. Blöchl, Projector augmented-wave method. *Phys. Rev. B* **50**, 17953-17979 (1994).
41. J. P. Perdew, K. Burke, M. Ernzerhof, Generalized gradient approximation made simple. *Phys. Rev. Lett.* **77**, 3865-3868 (1996).

SUPPLEMENTARY MATERIALS

Supplementary material for this article is available online

Table S1. Character table for C_{2v} and D_{3h}

Table S2. Nonlinear photocurrent responses under different polarized light

Fig. S1. Shift current and circular photocurrent in monolayer MX (C_{2v}) and 1H-MX_2 (D_{3h}) without spin orbit coupling

Fig. S2. Shift current and circular photocurrent in monolayer MX (C_{2v}) and 1H-MX_2 (D_{3h}) with spin orbit coupling

Fig. S3. Microscopic distribution and frequency dependent shift photocurrent susceptibility in monolayer 1H-$MoSe_2$ with D_{3h} point group
Fig. S4. Shift current and its microscopic origin in monolayer 1H-$MoSe_2$
Fig. S5. Group velocity v_x distribution in monolayer GeS
Fig. S6. Group velocity v_y distribution in monolayer GeS
Fig. S7. Berry curvature distribution in monolayer 1H-$MoSe_2$
Fig. S8. Shift current susceptibility tensor elements ($\sigma^{(2)}_{\mathrm{yxx}}$, $\sigma^{(2)}_{\mathrm{yyy}}$), and circular photocurrent susceptibility tensor elements ($\eta^{(2)}_{\mathrm{xyx}}$, $\eta^{(2)}_{\mathrm{xxy}}$) of monolayer GeS with and without scissor operator. The scissor operator is based on the bandgap correction using quasiparticle GW gap and exciton binding energy.

Acknowledgments: Funding: This research was supported by the National Science Foundation (NSF) under award number DMR-1753054. Portions of this research were conducted with the advanced computing resources provided by Texas A&M High Performance Research Computing. **Author contributions:** X.Q. conceived the project and supervised the research. H.W. and X.Q. developed first-principles codes for computing second-order nonlinear shift and circular photocurrent. H.W. performed the calculations. H.W. and X.Q. analyzed the results and wrote the manuscript. **Competing interests:** The authors declare that they have no competing interests. **Data and materials availability:** All data needed to evaluate the conclusions in the paper are present in the paper and/or the Supplementary Materials. Additional data related to this paper may be requested from the corresponding author.

Figure Captions and Tables

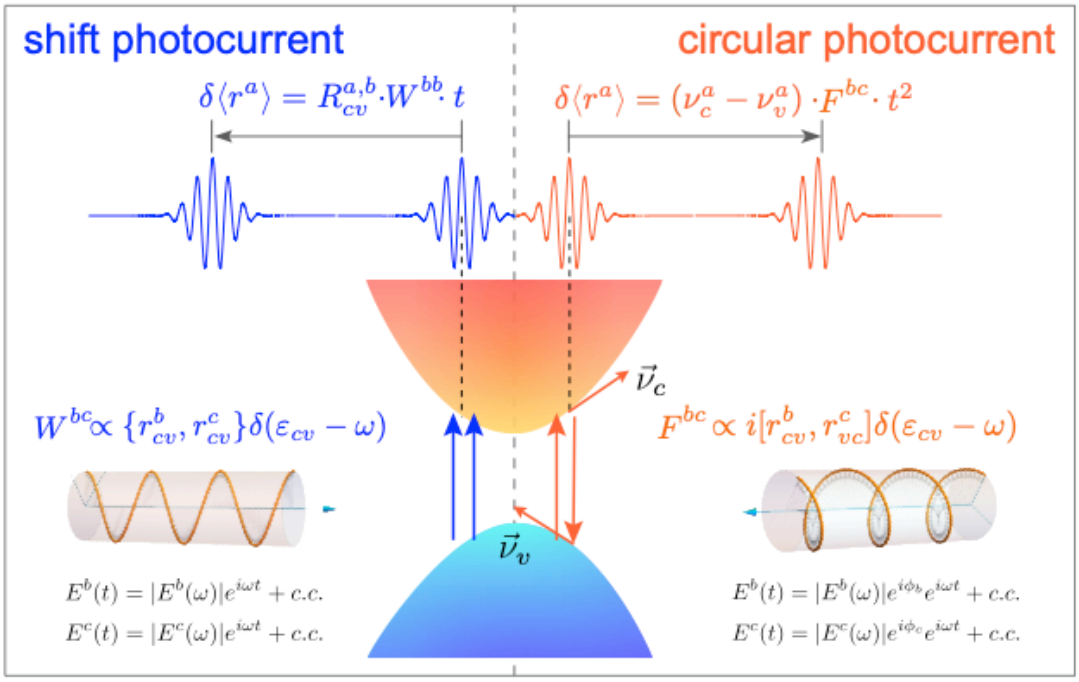

Fig. 1. Microscopic interpretation of shift current and circular current using two-band model. $\delta\langle r^a\rangle$ is the variation of the mean value of position operator indicating the shift of electron wave packet in real space. Photoexcitation induces the shift of the electron wave packet in real space. SC comes from the displacement of wave packet upon photoabsorption, while CC stems from the asymmetric motion of electrons and holes and the self-rotation of the wave packet. The latter induces itinerant orbital magnetic momentum coupled with the circularly polarized light. Transition rate *W* of SC is proportional to the linear optical absorption strength under linearly polarized light at frequency ω, while transition rate *F* of CC is proportional to the local Berry curvature under circularly polarized light at frequency ω.

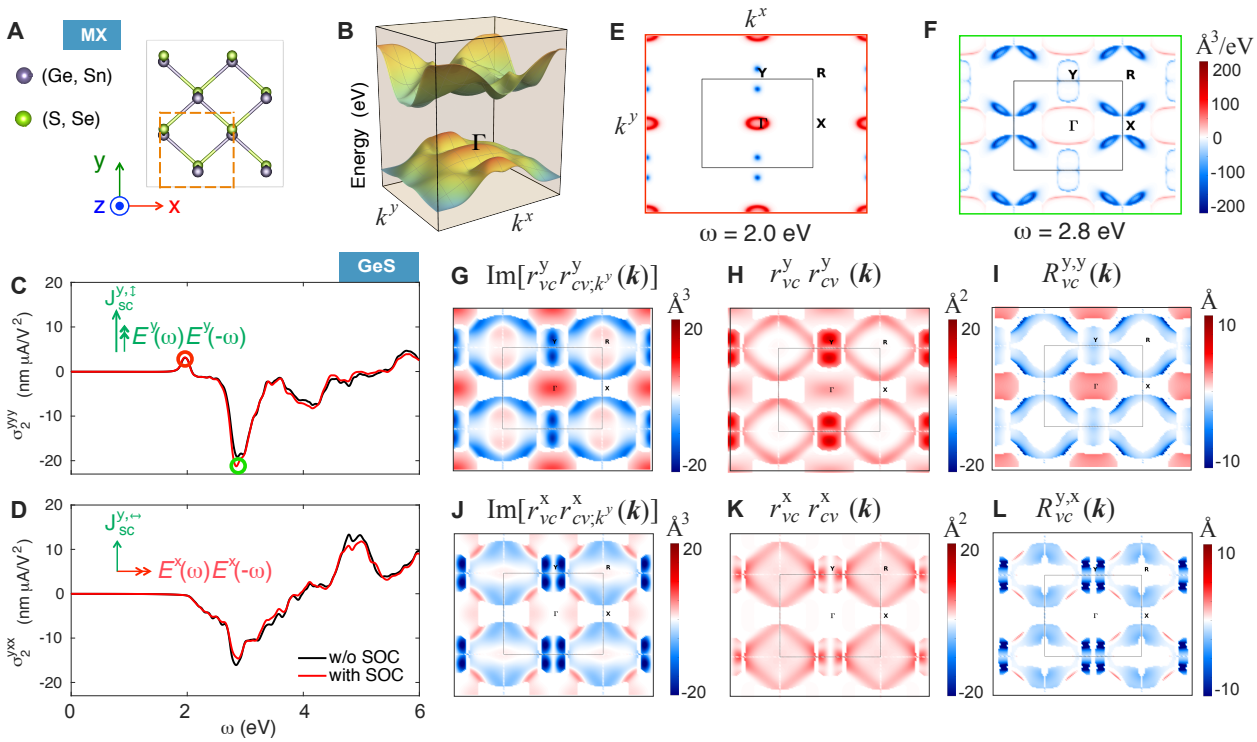

Fig. 2. Shift current (SC) and its microscopic origin in 2D ferroelastic-ferroelectric monolayer group IV monochalcogenide GeS. (**A**) Crystal structure of monolayer group IV monochalcogenides MX where M=(Ge, Sn) and X=(S, Se). (**B**) 2D electronic band structure near the Fermi level. (**C**) and (**D**) Frequency-dependent nonlinear shift current response to incoming linearly x and y polarized light, respectively. (**E**) and (**F**) Reciprocal vector ***k*** resolved SC susceptibility under linearly y polarized light at the first two peaks (2.0 and 2.8 eV). (**G**) and (**J**) ***k***-resolved SC strength, (**H**) and (**K**) ***k***-resolved dipole transition strength, (**I**) and (**L**) ***k***-resolved topological shift vector of 2D GeS in 2D Brillouin zone under linearly x and y polarized light, respectively.

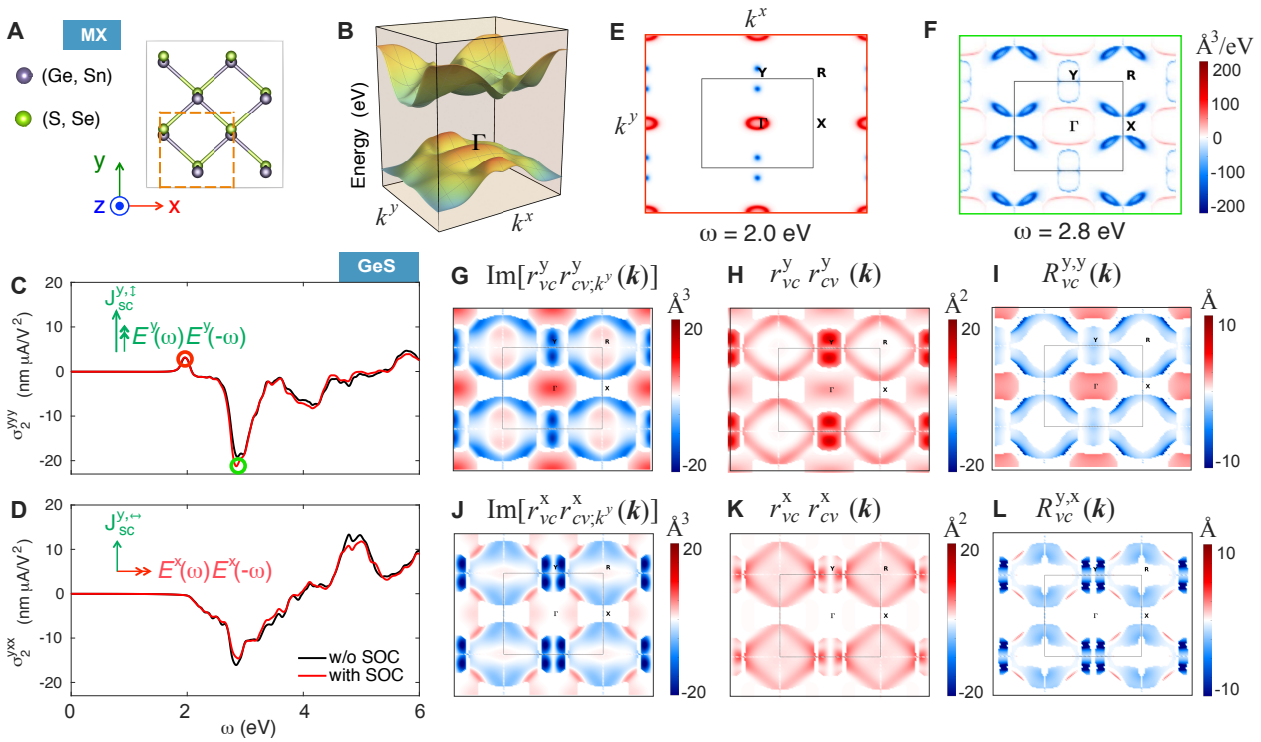

Fig. 2. Shift current (SC) and its microscopic origin in 2D ferroelastic-ferroelectric monolayer group IV monochalcogenide GeS. (**A**) Crystal structure of monolayer group IV monochalcogenides MX where M=(Ge, Sn) and X=(S, Se). (**B**) 2D electronic band structure near the Fermi level. (**C**) and (**D**) Frequency-dependent nonlinear shift current response to incoming linearly x and y polarized light, respectively. (**E**) and (**F**) Reciprocal vector ***k*** resolved SC susceptibility under linearly y polarized light at the first two peaks (2.0 and 2.8 eV). (**G**) and (**J**) ***k***-resolved SC strength, (**H**) and (**K**) ***k***-resolved dipole transition strength, (**I**) and (**L**) ***k***-resolved topological shift vector of 2D GeS in 2D Brillouin zone under linearly x and y polarized light, respectively.

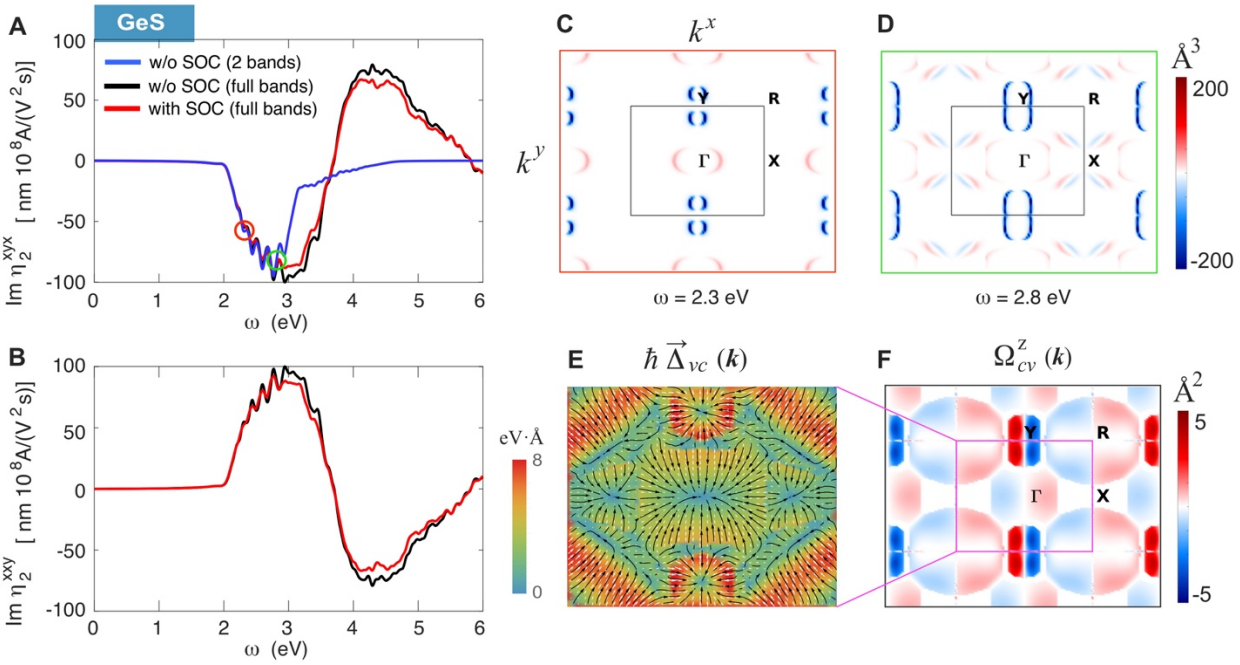

Fig. 3. Circular photocurrent (CC) and its microscopic origin in 2D ferroelastic-ferroelectric monolayer group IV monochalcogenide GeS. (**A**) and (**B**) Two opposite CC susceptibility tensor elements induced by circularly-polarized light. (**C**) and (**D**) Evolution of reciprocal vector ***k*** resolved CC susceptibility under circularly polarized light at two different frequencies (2.3 and 2.8 eV). (**E**) and (**F**) Group velocity difference and Berry curvature between the highest valence band and the lowest conduction band. The white arrows in (E) denote the calculated group velocity difference at specific ***k*** point, and the black curves indicate the associated stream lines.

Quantity	*Symmetry Operation*		*Gauge dependency*
	Space Inversion, $\boldsymbol{\mathcal{I}}$	Time Reversal, $\boldsymbol{\mathcal{T}}$	
$\boldsymbol{r}_{mn}(\boldsymbol{k})$	$-\boldsymbol{r}_{mn}(-\boldsymbol{k})$	$\boldsymbol{r}^{*}_{mn}(-\boldsymbol{k})$	Yes
$\boldsymbol{R}_{mn}(\boldsymbol{k})$	$-\boldsymbol{R}_{mn}(-\boldsymbol{k})$	$\boldsymbol{R}_{mn}(-\boldsymbol{k})$	No
$\boldsymbol{\Delta}_{mn}(\boldsymbol{k})$	$-\boldsymbol{\Delta}_{mn}(-\boldsymbol{k})$	$-\boldsymbol{\Delta}_{mn}(-\boldsymbol{k})$	No
$\boldsymbol{\Omega}_{mn}(\boldsymbol{k})$	$\boldsymbol{\Omega}_{mn}(-\boldsymbol{k})$	$-\boldsymbol{\Omega}_{mn}(-\boldsymbol{k})$	No

Table 1. Transformation of inter-band Berry connections $\mathbf{r}_{mn}$, shift vector $\mathbf{R}_{mn}$, group velocity difference $\boldsymbol{\Delta}_{mn}$ and Berry curvature $\boldsymbol{\Omega}_{mn}$ under space inversion $\boldsymbol{\mathcal{I}}$ and time reversal $\boldsymbol{\mathcal{T}}$ symmetry operation. $\boldsymbol{R}_{mn}(\boldsymbol{k})$ is odd under $\boldsymbol{\mathcal{I}}$ and even under $\boldsymbol{\mathcal{T}}$ in moment space. $\boldsymbol{\Omega}_{mn}(\boldsymbol{k})$ is even under $\boldsymbol{\mathcal{I}}$ and odd under $\boldsymbol{\mathcal{T}}$ in moment space. These transformation rules govern the coupling between ferroelectric polarization and nonlinear SC and CC photocurrent: $J_{\mathrm{SC}}^{y,\leftrightarrow}(P_y) = -J_{\mathrm{SC}}^{y,\leftrightarrow}(-P_y)$, $J_{\mathrm{SC}}^{y,\updownarrow}(P_y) = -J_{\mathrm{SC}}^{y,\updownarrow}(-P_y)$, $J_{\mathrm{CC}}^{x,\circlearrowleft}(P_y) = -J_{\mathrm{CC}}^{x,\circlearrowleft}(-P_y)$, and $J_{\mathrm{CC}}^{x,\circlearrowright}(P_y) = -J_{\mathrm{CC}}^{x,\circlearrowright}(-P_y)$.

Nonlinear photocurrent (J^x, J^y)			**ferroelectric order**			
			$+P$		$-P$	
			$+P_x$ if $\epsilon_{xx} > 0$	$+P_y$ if $\epsilon_{yy} > 0$	$-P_x$ if $\epsilon_{xx} > 0$	$-P_y$ if $\epsilon_{yy} > 0$
ferroelastic order	$+\epsilon$	$\epsilon_{xx} < 0$ & $\epsilon_{yy} > 0$	$\left(J_{\mathrm{CC}}^{\circlearrowleft,\circlearrowright}, J_{\mathrm{SC}}^{\leftrightarrow,\updownarrow}\right)$		$\left(-J_{\mathrm{CC}}^{\circlearrowleft,\circlearrowright}, -J_{\mathrm{SC}}^{\leftrightarrow,\updownarrow}\right)$	
	$-\epsilon$	$\epsilon_{xx} > 0$ & $\epsilon_{yy} < 0$	$\left(J_{\mathrm{SC}}^{\updownarrow,\leftrightarrow}, J_{\mathrm{CC}}^{\circlearrowleft,\circlearrowright}\right)$		$\left(-J_{\mathrm{SC}}^{\updownarrow,\leftrightarrow}, -J_{\mathrm{CC}}^{\circlearrowleft,\circlearrowright}\right)$	

Table 2. Ferroicity-driven nonlinear photocurrent switching. Second-order nonlinear photocurrent SC and CC responses are directly correlated with the intrinsic ferroic orders $(\pm P, \pm\epsilon)$ of 2D MX materials and external linear $(\leftrightarrow, \updownarrow)$ and circular $(\circlearrowleft, \circlearrowright)$ polarization of incoming light. Total 16 types of in-plane nonlinear photocurrents can be generated by controlling four ferroic states and four types of light polarizations.

Supplementary Materials for

Ferroicity-Driven Nonlinear Photocurrent Switching in Time-Reversal Invariant Ferroic Materials

Hua Wang[1], Xiaofeng Qian[1,*]

[1]Department of Materials Science and Engineering, Texas A&M University, College Station, TX 77843, USA

*Corresponding author. Email: feng@tamu.edu (X.Q.)

This PDF file includes:

1. Supplementary Tables

C_{2v}	E	$C_2(z)$	$\sigma_v(xz)$	$\sigma_v(yz)$	Basis function
A_1	+1	+1	+1	+1	z
A_2	+1	+1	-1	-1	R_z
B_1	+1	-1	+1	-1	x, R_y
B_2	+1	-1	-1	+1	y, R_x

D_{3h}	E	$2C_3(z)$	$3C_2'$	$\sigma_h(xy)$	$2S_3$	$3\sigma_v$	Basis function
A_1'	+1	+1	+1	+1	+1	+1	
A_2'	+1	+1	-1	+1	+1	-1	R_z
E'	+2	-1	0	+2	-1	0	(x, y)
A_1''	+1	+1	+1	-1	-1	-1	
A_2''	+1	+1	-1	-1	-1	+1	z
E''	+2	-1	0	-2	+1	0	(R_x, R_y)

Table S1. Character table for C_{2v} and D_{3h}

Light polarization	SC	CC
↔	$J_{\mathrm{SC}}^{\leftrightarrow} = 2\sigma_2^{yxx}E_0^2$	$J_{\mathrm{CC}}^{\leftrightarrow} = 0$
↕	$J_{\mathrm{SC}}^{\updownarrow} = 2\sigma_2^{yyy}E_0^2$	$J_{\mathrm{CC}}^{\updownarrow} = 0$
$\nearrow = \frac{(\leftrightarrow + \updownarrow)}{\sqrt{2}}$	$J_{\mathrm{SC}}^{\nearrow} = (\sigma_2^{yxx} + \sigma_2^{yyy})E_0^2$	$J_{\mathrm{CC}}^{\nearrow} = 0$
$\circlearrowleft = \frac{(\leftrightarrow + i\updownarrow)}{\sqrt{2}}$	$J_{\mathrm{SC}}^{\circlearrowleft} = (\sigma_2^{yxx} + \sigma_2^{yyy})E_0^2$	$J_{\mathrm{CC}}^{\circlearrowleft} = 2\mathrm{Im}\,\eta_2^{yxy}E_0^2$
$\circlearrowright = \frac{(\leftrightarrow - i\updownarrow)}{\sqrt{2}}$	$J_{\mathrm{SC}}^{\circlearrowright} = (\sigma_2^{yxx} + \sigma_2^{yyy})E_0^2$	$J_{\mathrm{CC}}^{\circlearrowright} = 2\mathrm{Im}\,\eta_2^{yyx}E_0^2 = -J_{\mathrm{CC}}^{\circlearrowleft}$

Table S2. Second order nonlinear photocurrent responses under different polarized light. ↔ and ↕ indicate horizontal (x) and vertical (y) linearly-polarized light, respectively. ↺ amd ↻ indicate left and right circularly polarized light, respectively. E_0 is the strength of the applied electric field. ↗ stands for linearly-polarized light that has a 45 degree angle with respect to x and y. Shift current (SC) and circular photocurrent (CC) can coexist in 2D MX (with C_{2v} point group) upon left/right circularly polarized light. However, only SC will persist, while CC will disappear in 2D MX under linearly polarized light such as ↔, ↕, and ↗,. It is important to mention that both SC and CC in monolayer MX_2 (e.g. 1H-$MoSe_2$ with D_{3h} point group) will be always zero under left/right circularly polarized light.

2. Supplementary Figures

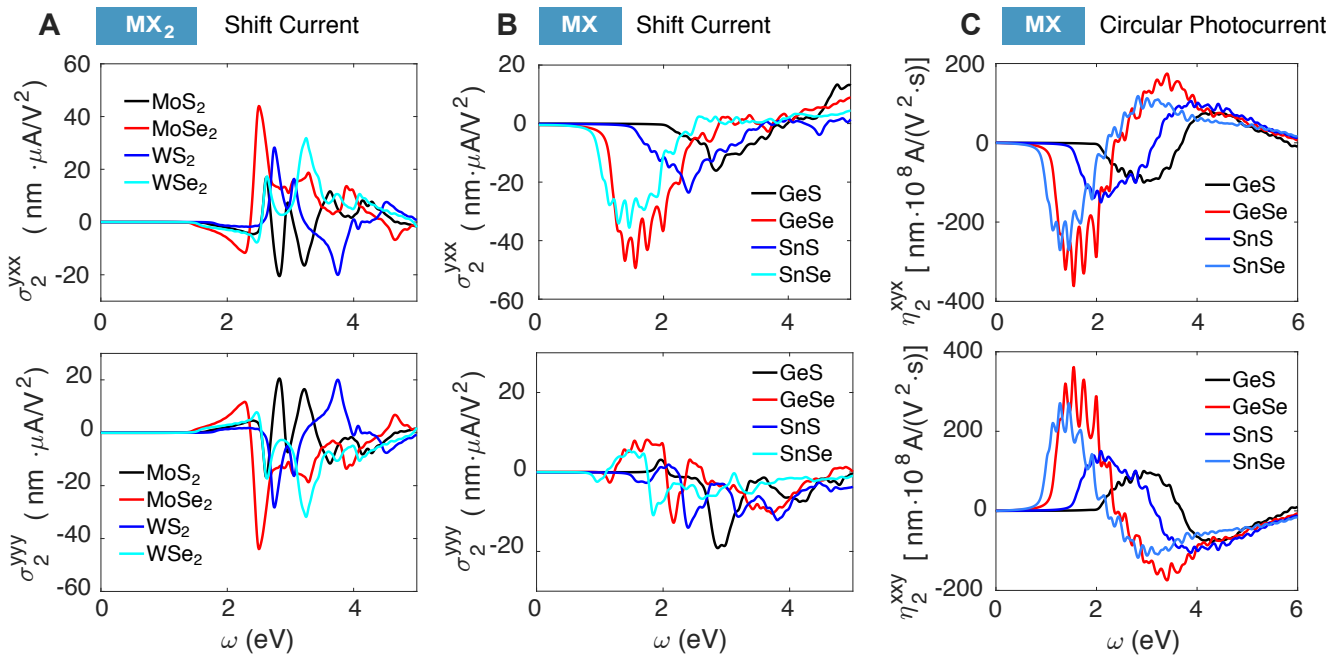

Fig. S1. Shift current and circular photocurrent in monolayer MX (C_{2v}) and 1H-MX_2 (D_{3h}) without spin orbit coupling. (**A**) Shift current susceptibility in 1H-MX_2. (**B**) Shift current susceptibility in MX. (**C**) Circular photocurrent susceptibility in MX.

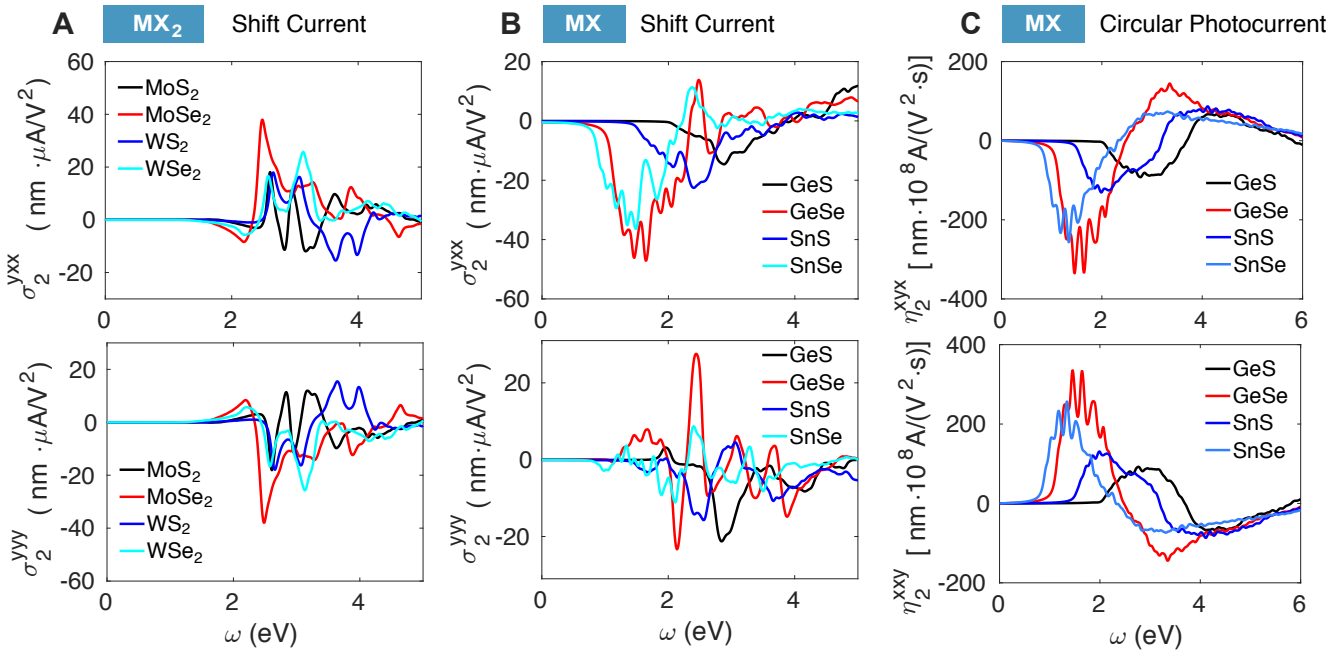

Fig. S2. Shift current and circular photocurrent in monolayer MX (C_{2v}) and 1H-MX_2 (D_{3h}) with spin orbit coupling. (**A**) Shift current susceptibility in 1H-MX_2. (**B**) Shift current susceptibility in MX. (**C**) Circular photocurrent susceptibility in MX.

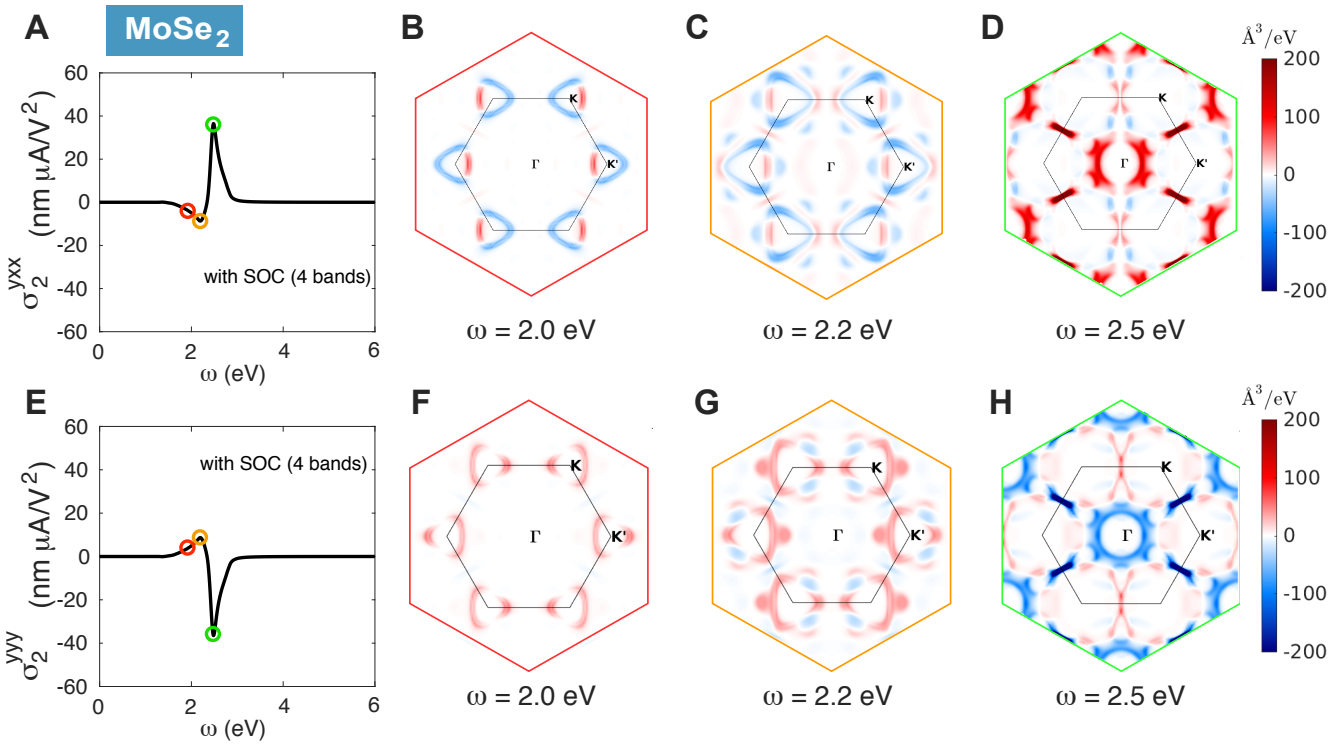

Fig. S3. Microscopic distribution and frequency dependent shift photocurrent susceptibility in monolayer 1H-$MoSe_2$ with D_{3h} point group. (**A, E**) Shift current susceptibility tensor elements σ_2^{yxx} and σ_2^{yyy} for shift current using four bands and SOC. (**B-D, F-H**) the distribution in k-space contributed to the susceptibility tensor element under incident light with different frequencies.

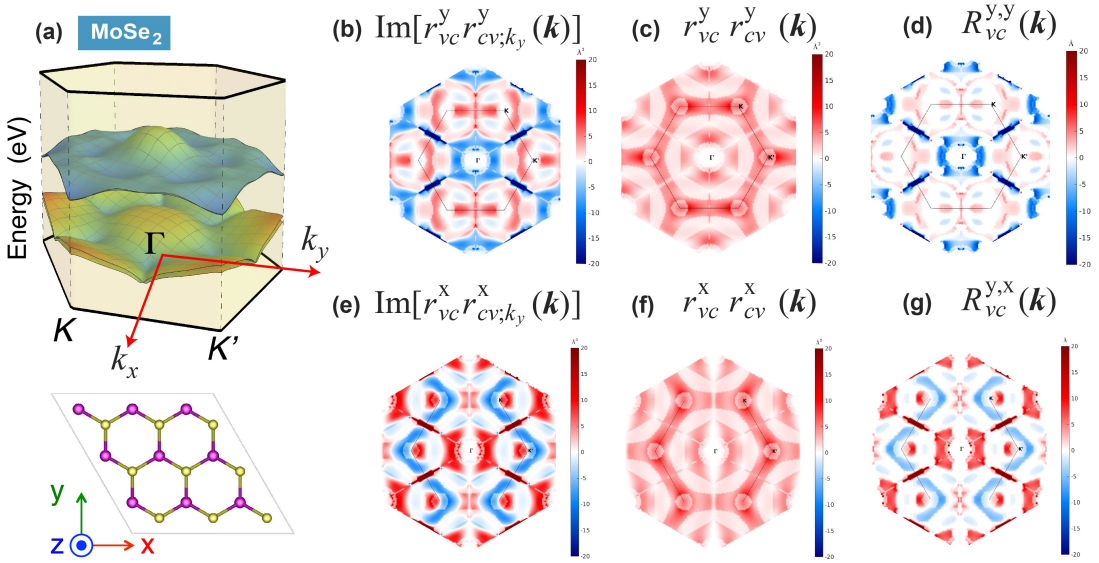

Fig. S4. Shift current and its microscopic origin in monolayer 1H-$MoSe_2$. (**A**) 2D electronic band structure near the Fermi level along with its crystal structure. (**B**) and (**E**) ***k***-resolved shift current strength, (**C**) and (**F**) ***k***-resolved dipole transition strength, (**D**) and (**G**) ***k***-resolved topological shift vector of monolayer 1H-$MoSe_2$ in 2D Brillouin zone under linearly x and y polarized light, respectively.

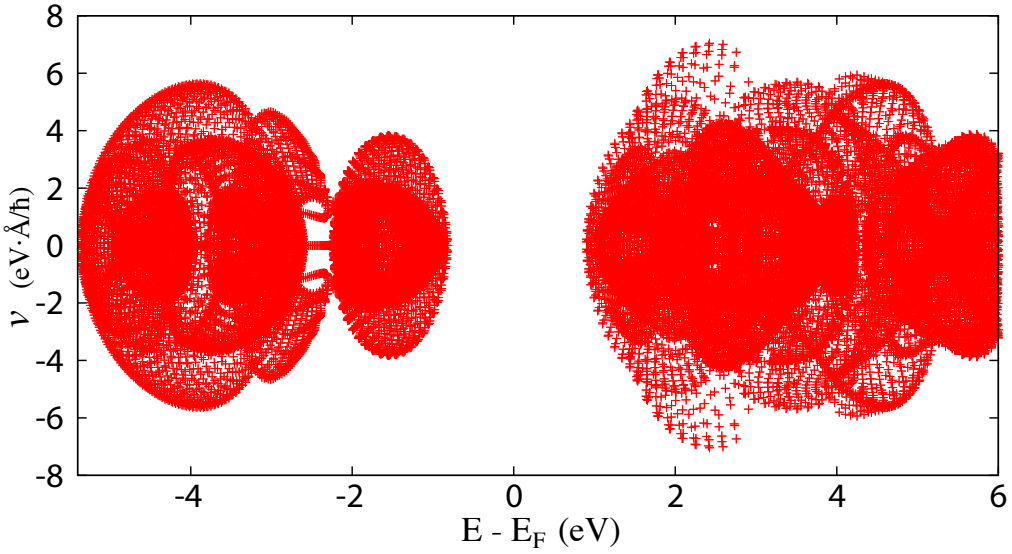

Fig. S5. Group velocity v_x distribution in monolayer GeS. The Fermi level is shifted to the middle of band gap.

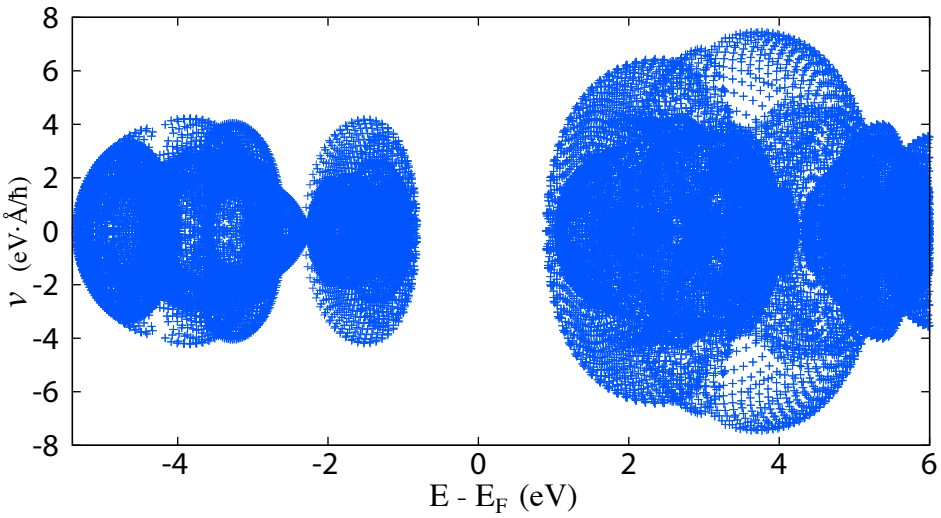

Fig. S6. Group velocity v_y distribution in monolayer GeS. The Fermi level is shifted to the middle of band gap.

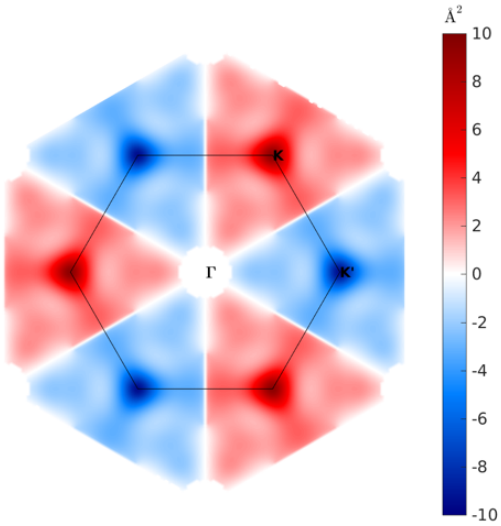

Fig. S7. Berry curvature distribution in monolayer 1H-$MoSe_2$.

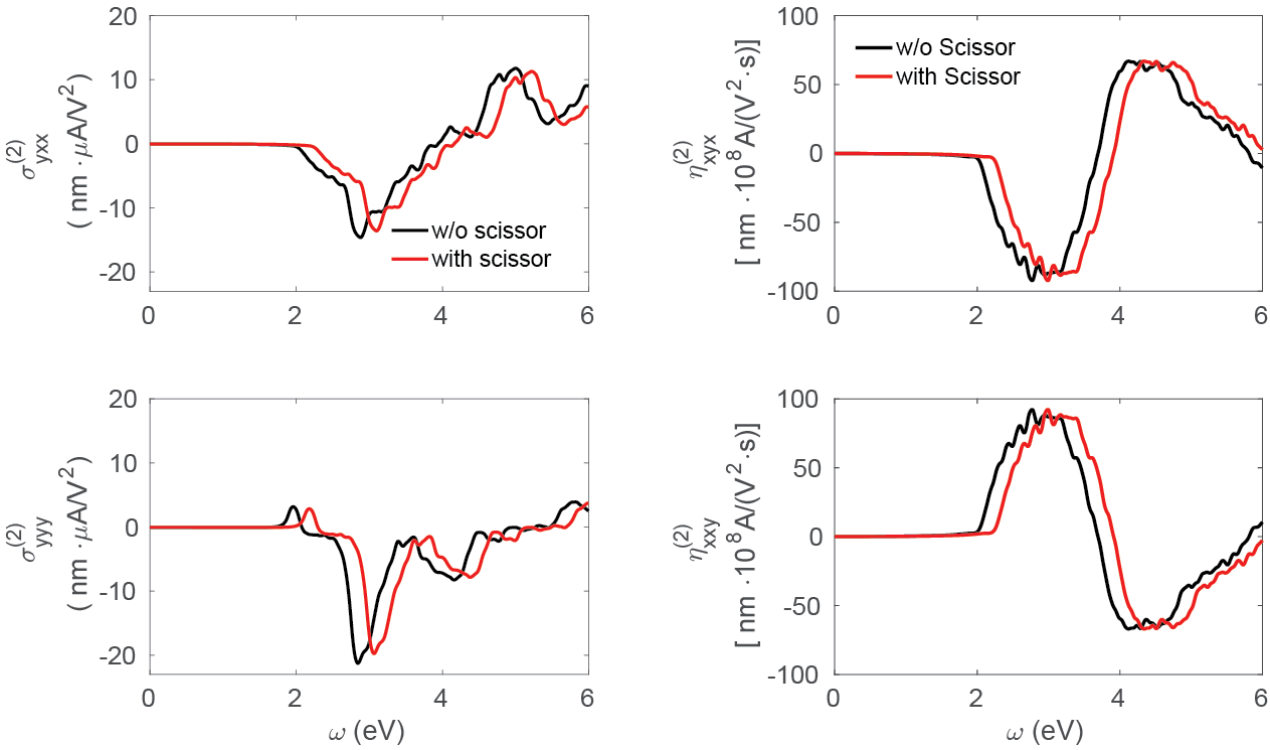

Fig. S8. Shift current susceptibility tensor elements ($\sigma^{(2)}_{yxx}$, $\sigma^{(2)}_{yyy}$), and circular photocurrent susceptibility tensor elements ($\eta^{(2)}_{xyx}$, $\eta^{(2)}_{xxy}$) of monolayer GeS with and without scissor operator. The scissor operator is based on the bandgap correction using quasiparticle GW gap and exciton binding energy.

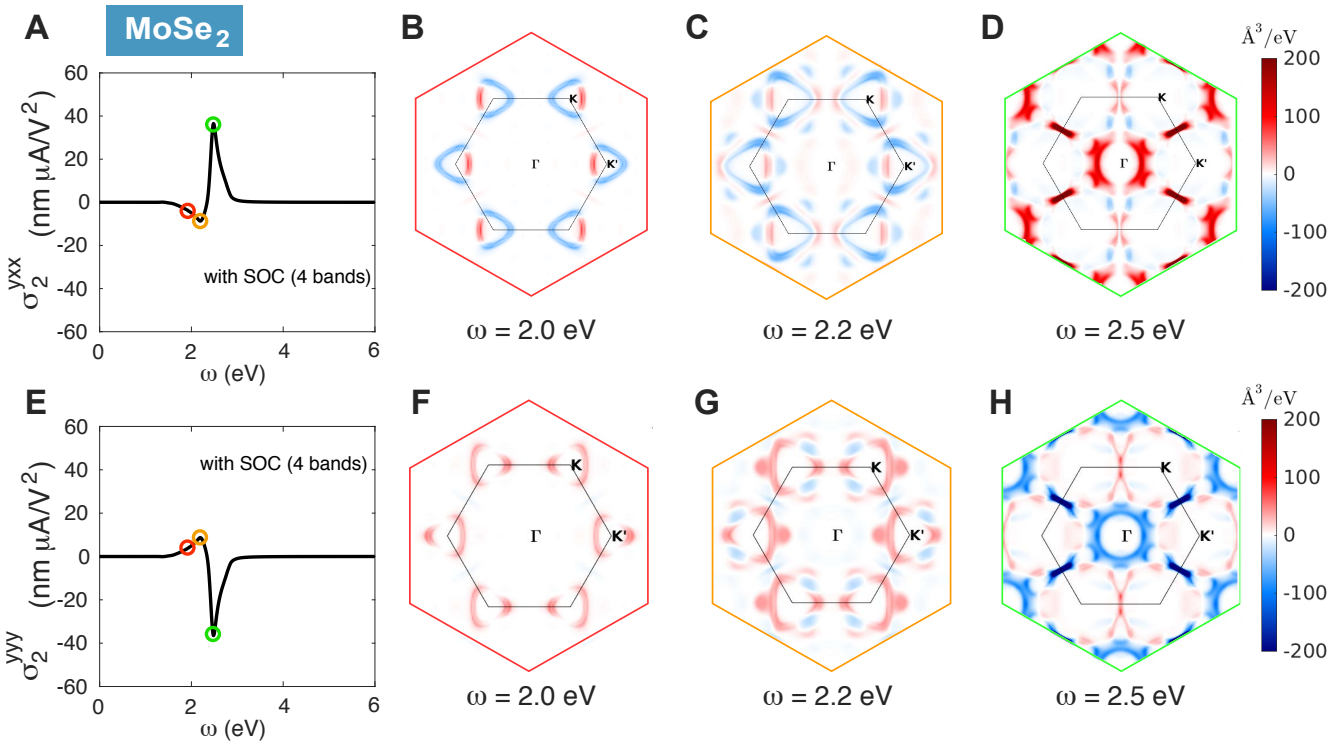

Fig. S3. Microscopic distribution and frequency dependent shift photocurrent susceptibility in monolayer 1H-$MoSe_2$ with D_{3h} point group. (**A, E**) Shift current susceptibility tensor elements σ_2^{yxx} and σ_2^{yyy} for shift current using four bands and SOC. (**B-D, F-H**) the distribution in k-space contributed to the susceptibility tensor element under incident light with different frequencies.

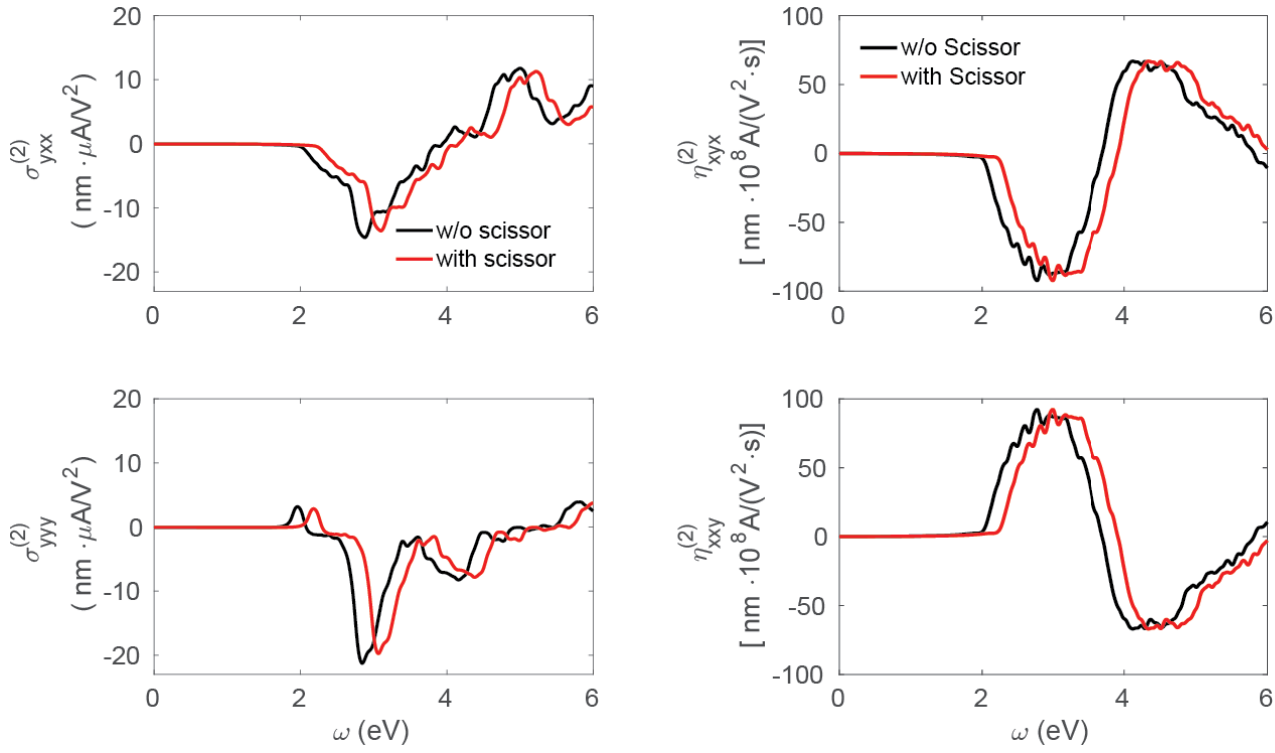

Fig. S8. Shift current susceptibility tensor elements ($\sigma^{(2)}_{yxx}$, $\sigma^{(2)}_{yyy}$), and circular photocurrent susceptibility tensor elements ($\eta^{(2)}_{xyx}$, $\eta^{(2)}_{xxy}$) of monolayer GeS with and without scissor operator. The scissor operator is based on the bandgap correction using quasiparticle GW gap and exciton binding energy.